Acta Crystallographica Section B
Structural Science
ISSN 0108-7681

Structure and phase transition of the Se-rich variety of antimonpearceite, $[(Ag,Cu)_6(Sb,As)_2(S,Se)_7]$-$[Ag_9Cu(S,Se)_2Se_2]$

Michel Evain,[a]* Luca Bindi[b] and Silvio Menchetti[b]

[a]Laboratoire de Chimie des Solides, IMN, UMR 6502 CNRS, Université de Nantes, 2 rue de la Houssinière, BP 32229, 44322 Nantes CEDEX 3, France, and [b]Dipartimento di Scienze della Terra, Università di Firenze, Via La Pira 4, I-50121 Firenze, Italy

Correspondence e-mail: michel.evain@cnrs-imn.fr

Received 10 March 2006
Accepted 14 June 2006

The crystal structure of a Se-rich antimonpearceite has been solved and refined by means of X-ray diffraction data collected at temperatures above (room temperature) and below (120 K) an ionic conductivity-induced phase transition. Both structure arrangements consist of the stacking of $[(Ag,Cu)_6(Sb,As)_2(S,Se)_7]^{2-}$ A (A') and $[Ag_9Cu(S,Se)_2Se_2]^{2+}$ B (B') module layers in which Sb forms isolated SbS_3 pyramids typically occurring in sulfosalts; copper links two S atoms in a linear coordination, and silver occupies sites with coordination ranging from quasi-linear to almost tetrahedral. In the ionic-conducting form, at room temperature, the silver d^{10} ions are found in the B (B') module layer along two-dimensional diffusion paths and their electron densities described by means of a combination of a Gram–Charlier development of the atomic displacement factors and a split-atom model. The structure resembles that of pearceite, except for the presence of both specific (Se) and mixed (S, Se) sites. In the low-temperature 'ordered' phase at 120 K the silver d^{10} ions of the B (B') module layer are located in well defined sites with mixed S—Se coordination ranging from quasi-linear to almost tetrahedral. The structure is then similar to that of 222-pearceite but with major differences, specifically its cell metric, symmetry and local arrangement in the B (B') module layer.

1. Introduction

Sulfosalts belonging to the pearceite–polybasite group, general formula $(Ag,Cu)_{16}M_2S_{11}$ with M = Sb, As, are relatively common in nature. Frondel (1963) divided this group of minerals into two series: pearceite-antimonpearceite, characterized by a 'small' unit cell [labelled 111] and high Cu content, and polybasite-arsenpolybasite, with doubled cell parameters [labelled 222] and low Cu content. Some years later an intermediate type of unit cell [labelled 221] was independently discovered by Harris *et al.* (1965), Edenharter *et al.* (1971) and Minčeva-Stefanova (1979). The $(Ag,Cu)_{16}(As,Sb)_2S_{11}$–$(Ag,Cu)_{16}(Sb,As)_2S_{11}$ system was also experimentally investigated by Hall (1967). This author studied the stability fields for all the members of the group and hypothesized that the chemical order–disorder phenomena observed in these minerals could be related to the different copper content.

From the chemical point of view, the members of both series are generally pure, only containing minor amounts of Bi, Pb, Zn, Fe. Nonetheless, Harris *et al.* (1965) reported the occurrence of an antimonpearceite sample from the San Carlos mine, Guanajuato, Mexico, containing up to 8.7 wt% of Se.

The crystal structure of pearceite was recently solved and refined in the $P\bar{3}m1$ space group by Bindi *et al.* (2006). They showed that the pearceite structure can be described as a

regular alternation of two kinds of layers stacked along the c axis: a first layer (labelled A), with general composition $[(Ag,Cu)_6(As,Sb)_2S_7]^{2-}$, and a second layer (labelled B), with general composition $[Ag_9CuS_4]^{2+}$. The complex polytypism phenomena (*i.e.* 221 and 222 unit cells) occurring in different polybasites were studied by Evain *et al.* (2006). These authors solved and refined the crystal structure of both polybasite-221 (space group $P321$) and polybasite-222 (space group $C2/c$) and proposed a possible mechanism regulating the type of unit cell that is stabilized in these minerals.

To confirm that pearceite and antimonpearceite possess the same type of crystal structure ($P\bar{3}m1$ space group) and to investigate the structural role of selenium in these minerals, a study of a Se-rich antimonpearceite crystal having a chemical composition of $(Ag_{14.67}Cu_{1.20}Bi_{0.01}Pb_{0.01}Zn_{0.01}Fe_{0.03})_{15.93}(Sb_{1.86}As_{0.19})_{2.05}(S_{8.47}Se_{2.55})_{11.02}$ was undertaken. Recent experiments conducted by the present authors (currently in progress) showed these compounds to be good ionic conductors down to well below room temperature. In particular, conductivity as well as DSC measurements performed on pure antimonpearceite powders showed an anomalous behaviour at approximately 273 K, thus indicating a possible phase transition. Unfortunately, owing to the scarcity of the sample, the same set of experiments could not be carried out on the selenium-rich variety. However, since the close similarity in the chemical composition with the pure antimonpearceite, it seems reasonable to assume that a similar behaviour could also occur in the sample studied here.

This paper reports the structure determination of the Se-rich antimonpearceite in both the ionic-conducting phase found above ~273 K and the low-temperature superstructure occurring below ~273 K.

2. Occurrence and chemical composition

The sample (mineralogical collection of the Natural History Museum of the University of Firenze catalogue number 2453/I) containing the Se-rich antimonpearceite is from the De Lamar mine, Idaho, USA. The mineral occurs as anhedral to subhedral grains up to 350 μm across and shows a grey–black to black streak. It does not show any inclusions of other minerals or intergrowths. Associated minerals are naumannite, covellite and pyrite, whereas the gangue mineral is calcite.

A preliminary chemical analysis using energy-dispersive spectrometry, performed on the crystal fragments used for the structural study, did not indicate the presence of elements (Z > 9) other than S, Fe, Cu, Zn, As, Se, Ag, Sb, Pb and Bi. The chemical composition was then determined using wavelength-dispersive analysis by means of a Jeol JXA-8200 electron microprobe. Major and minor elements were determined at a 20 kV accelerating voltage and a 40 nA beam current, with 10 s as counting time. For the wavelength-dispersive analyses the following lines were used: S $K\alpha$, Fe $K\alpha$, Cu $K\alpha$, Zn $K\alpha$, As $L\alpha$, Se $L\alpha$, Ag $L\alpha$, Sb $L\beta$, Pb $M\alpha$, Bi $M\beta$. The standards employed were native elements for Cu and Ag, galena for Pb, pyrite for Fe and S, synthetic Sb_2S_3 for Sb, synthetic As_2S_3 for As, synthetic Bi_2S_3 for Bi, synthetic ZnS for Zn, and synthetic $PtSe_2$ for Se. The crystal fragment was found to be homogeneous within analytical error. The average chemical composition (ten analyses on different spots), together with ranges of wt% of elements, are reported in Table 1. On the basis of 29 atoms, the chemical formula can be written as $(Ag_{14.67}Cu_{1.20}Bi_{0.01}Pb_{0.01}Zn_{0.01}Fe_{0.03})_{15.93}(Sb_{1.86}As_{0.19})_{2.05}(S_{8.47}Se_{2.55})_{11.02}$.

Table 1
Electron microprobe data (means and ranges in wt% of elements) and atomic ratios with their standard deviations (σ) for the Se-rich antimonpearceite crystal.

	wt%	Range	Atomic ratios	σ
Ag	66.17	65.21–67.39	14.67	0.14
Cu	3.19	2.88–3.81	1.20	0.07
Bi	0.09	0.00–0.16	0.01	0.01
Pb	0.09	0.02–0.20	0.01	0.01
Zn	0.03	0.00–0.09	0.01	0.01
Fe	0.07	0.00–0.12	0.03	0.01
Sb	9.47	9.00–9.89	1.86	0.09
As	0.60	0.23–0.99	0.19	0.02
S	11.36	10.88–11.56	8.47	0.08
Se	8.42	8.01–8.77	2.55	0.06
Total	99.49	99.11–100.26		

3. Structure determination

3.1. Data collection

A Se-rich antimonpearceite crystal was isolated from a ground sample for both the room temperature (RT) and low-temperature (120 K, well below the phase-transition temperature) data collections. The intensity measurements were carried out on a Bruker–Nonius Kappa CCD diffractometer, using graphite-monochromated Mo K–$L_{2,3}$ radiation (λ = 0.71073 Å). For the 120 K analysis, the low temperature was achieved by means of an Oxford cryostream cooler. Because of the suspected ionic conductivity at RT and the probable twinning for the low-temperature phase, a rather high $\sin\theta/\lambda$ cut-off and a full sphere exploration were considered. At RT as well as at 120 K the symmetry appeared as trigonal ($\bar{3}m1$ point group) with cell parameters $a_h \simeq 7.60$ Å and $c_h \simeq 12.07$ Å and supercell parameters $a_{hs} = 2a_h \simeq 15.18$ Å and $c_{hs} = 2c_h \simeq 23.73$ Å at RT and 120 K, respectively. Intensity integration and standard Lorentz-polarization correction were performed with the Bruker–Nonius EvalCCD program package.

3.2. Data reduction and refinement at RT

The RT data set was corrected for the absorption by an analytical Gaussian integration based upon the crystal shape and dimension which were first optimized using *X-shape* (Stoe & Cie, 1996), based on the *Habitus* program (Herrendorf, 1993). Subsequent calculations were carried out using the *Jana2000* program suite (Petricek & Dusek, 2000). Averaging according to the $\bar{3}m1$ point group gave an internal R value of 0.0456.

Table 2
Crystallographic data for the selected Se-rich antimonpearceite crystal.

	300 K	120 K
Crystal data		
Chemical formula	$Ag_{14.59}As_{0.34}Cu_{1.41}S_{8.34}Sb_{1.66}Se_{2.66}$	$Ag_{14.69}Cu_{1.31}S_{8.37}Sb_2Se_{2.63}$
M_r	2368.3	2387.5
Cell setting, space group	Trigonal, $P\bar{3}m1$	Monoclinic, $P12_1/c1$
Temperature (K)	300	120
a, b, c (Å)	7.5950 (4), 7.5950 (4), 12.0731 (6)	13.1426 (14), 7.5879 (7), 23.729 (4)
α, β, γ (°)	90, 90, 120	90, 90, 90
V (Å^3)	603.12 (5)	2366.4 (5)
Z	1	4
D_x (Mg m^{-3})	6.518	6.699
Radiation type	Mo $K\alpha$	Mo $K\alpha$
No. of reflections for cell parameters	156	164
μ (mm^{-1})	19.67	20.02
Crystal form, colour	Block, black	Block, black
Crystal size (mm)	0.10 × 0.07 × 0.04	0.10 × 0.07 × 0.04
Data collection		
Diffractometer	KappaCCD	KappaCCD
Data collection method	CCD, ω frames	CCD, φ and ω frames
Absorption correction	Gaussian	Gaussian
T_{min}	0.157	0.137
T_{max}	0.523	0.363
No. of measured, independent and observed reflections	13 591, 1253, 975	151 079, 27 670, 21 308
Criterion for observed reflections	$I > 2\sigma(I)$	$I > 2\sigma(I)$
R_{int}	0.046	0.085
θ_{max} (°)	38.0	36.0
Refinement		
Refinement on	F	F
$R[F^2 > 2\sigma(F^2)]$, $wR(F^2)$, S	0.049, 0.060, 1.80	0.069, 0.076, 1.80
No. of parameters	95	269
Weighting scheme	Based on measured s.u.'s, $w = 1/[\sigma^2(F) + 0.0004F^2]$	Based on measured s.u.'s, $w = 1/[\sigma^2(F) + 0.000484F^2]$
$(\Delta/\sigma)_{max}$	<0.0001	0.001
$\Delta\rho_{max}$, $\Delta\rho_{min}$ (e Å^{-3})	0.79, −0.64	5.51, −2.74
Extinction method	B-C type 2 (Becker & Coppens, 1974)	None
Extinction coefficient	0.332272	

Computer programs: *Jana2000* (Petricek & Dusek, 2000).

Starting from the pearceite structure model (Bindi *et al.*, 2006), the refinement converged smoothly. The sites with complete (Se site) or partial (S1/Se1′ and S3/Se3′ sites) substitution of S by Se were easily identified. To mimic the silver (Ag2 and Ag3) electron spreading along diffusion paths and to model the selenium (Se4) distribution, up to fourth-order non-harmonic Gram–Charlier tensors were used for the Debye–Waller description (Johnson & Levy, 1974; Kuhs & Heger, 1979). Similarly, third- and fourth-order tensors were introduced for the description of Ag1b/Cu1b and S3/Se3′ partial substitutions, respectively.

Full site occupation (Sb/As, Ag1a/Ag1b/Cu1b, S1/Se1′ and S3/Se3′) was assured through constraints and the overall charge balance was ascertained. Adding a secondary extinction coefficient (Becker & Coppens, 1974), the final residual values converged at R = 0.0489 (wR = 0.0575) for 975 independent observed reflections [$2\sigma(I)$ level] and 94 parameters and R = 0.0768 (wR = 0.0596) for all 1253 independent reflections. Crystal characteristics, data collection and reduction parameters, and refinement results are gathered in Table 2. Atomic parameters are available in the supplementary data[1] and in Table 3.

Table 3
Higher-order displacement parameters and s.u.'s for the selected Se-rich antimonpearceite crystal.

Third-order tensor elements C^{ijk} are multiplied by 10^3. Fourth-order tensor elements D^{ijkl} are multiplied by 10^4.

	Ag1b/Cu1b′	Ag3	Se
300 K			
C^{111}	0.092 (9)	0.023 (5)	−0.0043 (7)
C^{112}	0.046 (5)	0.109 (7)	−0.0021 (4)
C^{113}	0.024 (3)	−0.0037 (11)	0.0031 (4)
C^{122}	0.017 (3)	0.205 (12)	0.0021 (4)
C^{123}	0.0121 (16)	−0.0080 (17)	0.00157 (19)
C^{133}	0.012 (2)	−0.0023 (5)	0
C^{222}	0.002 (5)	0.05 (4)	0.0043 (7)
C^{223}	0.0077 (13)	−0.001 (4)	0.0031 (4)
C^{233}	0.0058 (11)	0.0002 (9)	0
C^{333}	0.0011 (15)	−0.0020 (5)	0.0002 (3)

	Ag3	S3/Se3′
D^{1111}	0.048 (7)	−0.36 (4)
D^{1112}	0.091 (9)	−0.180 (18)
D^{1113}	−0.0046 (16)	−0.028 (9)
D^{1122}	0.138 (13)	−0.180 (18)
D^{1123}	−0.005 (2)	−0.014 (4)
D^{1133}	0.0010 (5)	0.000 (3)
D^{1222}	0.16 (2)	−0.180 (18)
D^{1223}	−0.002 (3)	0.014 (4)
D^{1233}	0.0011 (6)	0.0002 (15)
D^{1333}	0.0000 (3)	0
D^{2222}	−0.34 (5)	−0.36 (4)
D^{2223}	0.075 (8)	0.028 (9)
D^{2233}	−0.0100 (15)	0.000 (3)
D^{2333}	−0.0007 (5)	0
D^{3333}	0.0015 (4)	0.0007 (17)

3.3. Data reduction and refinement at 120 K

The 120 K data set was corrected for the absorption by an analytical Gaussian integration based upon the previously determined crystal shape. With cell parameters (2a and 2c) approximately corresponding to those of polybasite-222 (Evain *et al.*, 2006), a structure model equivalent to that of polybasite-222 was looked for, that is, in the monoclinic system (orthohexagonal supercell: $\mathbf{a}_{ms} = 2\mathbf{a}_{hs} + \mathbf{b}_{hs}$, $\mathbf{b}_{ms} = \mathbf{b}_{hs}$ and $\mathbf{c}_{ms} = \mathbf{c}_{hs}$), space group $C2/c$. This approach failed, whatever the twin law considered in addition to the obvious threefold axis. All the possible space-group/twinning-law combinations were then explored, keeping in mind that the *hkl* systematic absence rules could be destroyed through twinning reflection overlap. It should be noted that the starting model derived from the higher-temperature solution corresponds to about

[1] Supplementary data for this paper are available from the IUCr electronic archives (Reference: LC5047). Services for accessing these data are described at the back of the journal.

350 independent atoms in the 2 × 2 × 2 cell (*P*1 symmetry). Among them about half are Ag atoms found along the diffusion paths, with site occupancy factors to be refined to give either a full occupancy and be kept or a zero occupancy and be removed. To simplify the structure determination, all mixed S/Se sites were considered as fully occupied by sulfur.

Lowering the symmetry to *P*1 and refining the structure with rigid constraints on atomic displacement parameters and a drastic damping factor (as low as 0.01), a partial solution was finally found after several attempts and analyzed by means of the *PLATON* program (Spek, 1990). The analysis revealed non-crystallographic pseudo-translation symmetries, which were considered as the indication of a wrong cell selection. Up to this point, only twinning by metric merohedry had been considered, that is with twin index $n_T = 1$ (Nespolo, 2004, and references therein). Going back to the diffraction pattern, it was realised that a twinning by reticular merohedry should also be considered. Indeed, all the measured reflections could be gathered into a single set by taking into account a primitive cell of dimension $\mathbf{a}_m = \mathbf{a}_{hs} + \mathbf{b}_{hs}/2$, $\mathbf{b}_m = \mathbf{b}_{hs}/2$ and $\mathbf{c}_m = \mathbf{c}_{hs}$ and a threefold twin axis. A search for symmetry operations in that new cell then led to the $P2_1/c$ space group. It is worth noting that the systematic extinctions corresponding to this space group do not appear in the diffraction pattern, owing to the twinning reflection overlap.

With the correct cell, space group and twin law the refinement converged smoothly without damping factor. S/Se substitution was then introduced on the mixed sites revealed in the higher-temperature phase, *i.e.* S1/Se1′, S2/Se2′ and S9/Se9′. The analysis of the distances (see structure description) revealed the Ag sites with partial Cu substitution. At the final stage, small but significant positive residues (up to ∼5 e^- Å^{-3}) were left unexplained in the difference Fourier synthesis maps. Those residues were found in the vicinity of atoms already introduced in the structure model, especially Sb atoms in the *A* module layer (see structure description). Several additional twin laws were then considered, but none could significantly lower the residual maxima. The positive residues probably correspond to the existence of stacking faults, as already observed in the structure determination of the 221-polybasite (Evain *et al.*, 2006). Indeed, an attempt to introduce stacking faults (*c*/2 translation) in the refinement by means of a rigid body slightly lowered the positive residue values (down to ∼4 e^- Å^{-3}), which were then found around the Ag atoms in the *B* layer, with only a tiny residual *R*-value improvement. It is worth noting that the stacking fault ratios and types are not necessarily the same in the three twin domains but they are, however, inherently considered as equivalent by the refinement procedure. Given the very small gain in the agreement factor and the complication in the structure report, it was decided to consider a final model without stacking faults. The only perturbation that the positive residues, found around Sb atoms in the difference Fourier maps, introduce in the final structure model is to bias the overall stoichiometry since it is not possible to partly substitute Sb by the lighter element As, as both the elemental analysis and the RT refinement suggest. Indeed, a tentative refinement of the Sb/As ratio yielded a >100% Sb occupation! Higher-order Debye–Waller tensors for the mixed Ag5/Cu5′ sites and for atoms in the neighborhood of mixed S/Se′ sites (Ag9 and Ag10) were not considered since they would be meaningless given the stacking faults.

The residual values converged at $R = 0.0692$ ($wR = 0.0731$) for 21308 independent observed reflections [$2\sigma(I)$ level] and 269 parameters and $R = 0.0994$ (Rw = 0.0758) for all 27670 independent reflections. Crystal characteristics, data collection and reduction parameters, and refinement results are gathered in Table 2. Atomic parameters are reported in the supplementary data.

4. Structure description

4.1. Higher-temperature structure

In its higher-temperature ionic-conducting form, the Se-rich antimonpearceite structure resembles that of pearceite (Bindi *et al.*, 2006). It can be described as the alternation, along the *c* axis, of two pseudo-layer modules: an $[(Ag,Cu)_6(Sb,As)_2(S,Se)_7]^{2-}$ *A* module layer and an $[Ag_9Cu(S,Se)_2Se_2]^{2+}$ *B* module layer (Fig. 1*a*). Structure drawings were realised using the *Diamond* program (Brandenburg, 2001) and the *IRIS Explorer* visualization program (Numerical Algorithms Group) running on a Compaq DS20 computer.

In the *A* module layer, the Ag atoms are triangularly coordinated by S atoms in a quasi-planar environment. Since silver is partially substituted by copper (Ag1b/Cu1b′) and sulfur by selenium (S3/Se3′), we have used a Gram–Charlier description of the Debye–Waller factor in the structure refinement. For the same reason, the calculated distances are only average distances and are not, therefore, useful pieces of information (a thorough discussion on distances will be made for the lower-temperature structure; see below). The (Sb,As)

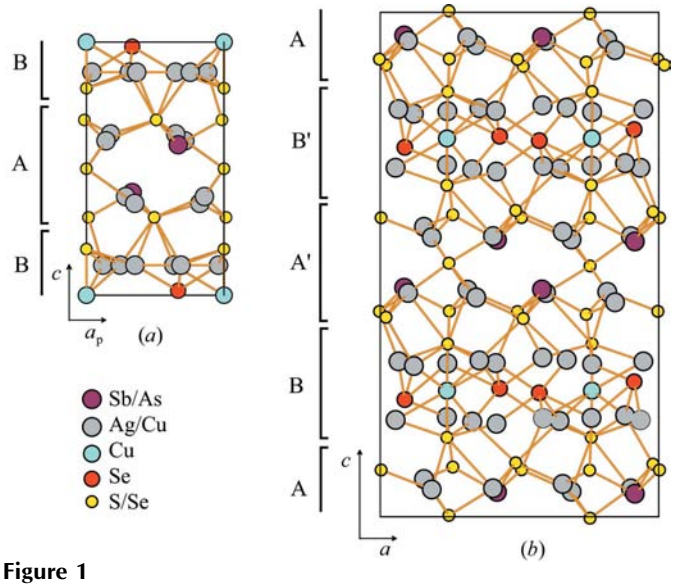

Figure 1
Projection of the higher-temperature (*a*) and lower-temperature (*b*) Se-rich antimonpearceite structure along the hexagonal and monoclinic *b* axis, respectively. The figure emphasizes the alternation of the $[(Ag,Cu)_6(Sb,As)_2(S,Se)_7]^{2-}$ *A* (*A*′) and $[Ag_9Cu(S,Se)_2Se_2]^{2+}$ *B* (*B*′) module layers.

atoms are also in a threefold coordination, but in a trigonal pyramidal configuration. The [AgS_3] and [SbS_3] subunits are linked together through corners to constitute the *A* module layer.

In the *B* module layer, the silver d^{10} cations are distributed along two-dimensional diffusion paths, in a structure skeleton made of face-sharing tetrahedra (as in argyrodite ionic-conducting compounds; Boucher *et al.*, 1992, 1993) around the Cu atom (see Fig. 2). Each diffusion path is based upon hexagonal-like cycles interconnected through lower-density bridges (see Fig. 3). It is worth noting that the modes (maxima of density) observed in the diffusion paths do not correspond to the Ag refined positions and that there are no atomic positions in the connexions, the Gram–Charlier expansion of the Debye–Waller factor providing the connecting density. For that reason the refined positions should not be used to calculate distances (though meaningful distances could be obtained with mode positions). The Se atom in the middle of the *B* module layer, along with the Cu atom, is purely selenium, while the S1 atom linearly coordinating Cu is partially substituted by selenium. This accounts for the Cu—S1/Se1′ distance [2.291 (2) Å] being longer than the Cu—S distance [2.161 (3) Å; Bindi *et al.*, 2006].

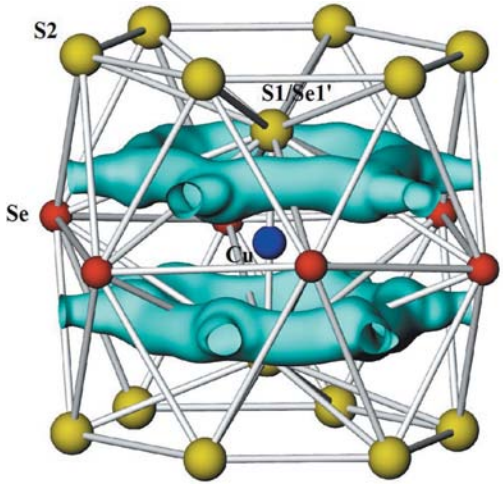

Figure 2
Non-harmonic joint probability density isosurface of silver for Se-rich antimonpearceite at room temperature. S, Se and Cu atoms are drawn at an arbitrary size. Level of the three-dimensional map: 0.05 Å^{-3}. The figure illustrates the silver diffusion in the *ab* plane among the various S/Se tetrahedral sites.

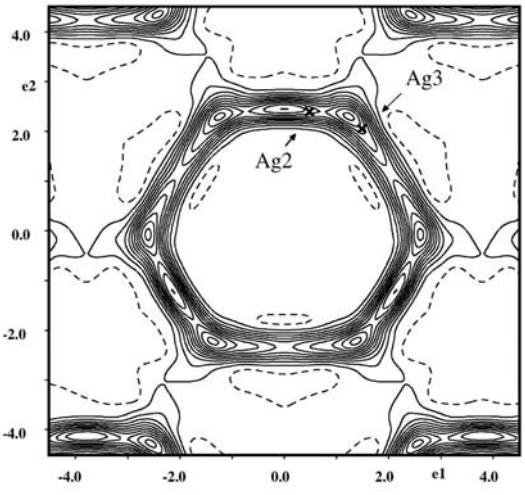

Figure 3
Non-harmonic joint probability density function map showing the silver diffusion path at room temperature in the *ab* plane. Map in Å, centred at (0,0,0.12) and summed over Δz = 2 Å. Positive contour lines in intervals of 0.03 Å^{-3}. Negative contours at −0.01 Å^{-3} indicated by dashed lines. Refined positions indicated by *x*.

4.2. Lower-temperature (120 K) structure

At the transition toward the lower-temperature form, the Ag d^{10} ions, which are found in the diffusion paths of the higher-temperature form, order in well defined positions. This ordering implies a lowering of symmetry, along with a cell enlargement. Starting with the $P\bar{3}m1$ trigonal space group there is no direct group–subgroup relation going to the $P2_1/c$ space group. Indeed, three steps have to be used: an isomorphic transformation to the same $P\bar{3}m1$ space group (subgroup of type IIc), corresponding to the doubling of the *c* axis, then a transformation to the *translationengleiche* *C*2/*m* subgroup (subgroup of type I), and finally a transformation to the *klassengleiche* $P2_1/c$ subgroup (subgroup of type IIa). It should be noticed that the final space group and cell metric are different from that observed for 222-polybasite (Evain *et al.*, 2006). As found in 222-polybasite, there is a doubling along the *c* axis with, therefore, the alternation of two different *A*–*B* module double layers (*A*–*B* and *A*′–*B*′, see Fig. 1*b*) which are related by an inversion center. However, within the *ab* plane the ordering requires a smaller periodicity than in the 222- or 221-polybasite. The reason for the difference can be seen in Fig. 4 where the Se-rich antimonpearceite and 221-polybasite *B* module layers are compared (the 222-polybasite *B* layer is similar to that 221-polybasite, but with a monoclinic

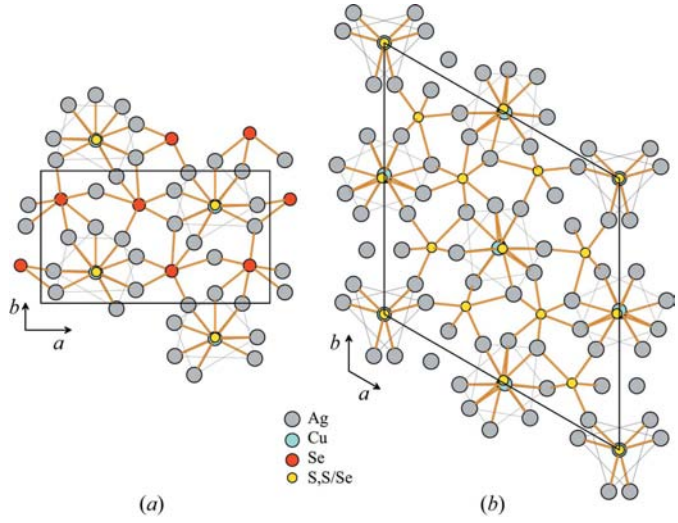

Figure 4
Projection along the *c* axis of (*a*) the $[Ag_9Cu(S,Se)_2Se_2]^{2+}$ *B* (*B*′) module layer of the lower-temperature Se-rich antimonpearceite structure and (*b*) the $[Ag_9CuS_4]^{2+}$ *B* (*B*′) module layer of the 221-polybasite structure (Evain *et al.*, 2006). The sulfur environment around Cu is highlighted by thin S–S connecting lines.

Table 4
Main interatomic distances (Å) and s.u.'s, weighted mean distance (Å) and ^{n}ECoN for the selected Se-rich antimonpearceite crystal.

For ^{n}ECoN, see definitions given by Hoppe (1979) and Nespolo *et al.* (2001).

$[(Ag,Cu)_6(Sb,As)_2(S,Se)_7]^{2-}$ *A* layer:					
Sb1—S3	2.4093 (18)	Sb2—S8	2.4150 (18)	Ag1—S6	2.4962 (18)
Sb1—S6	2.4173 (17)	Sb2—S4	2.4160 (18)	Ag1—S9/Se9′	2.537 (2)
Sb1—S5	2.4197 (18)	Sb2—S7	2.4231 (17)	Ag1—S5	2.5986 (19)
				Ag1—S1/Se1′	3.2315 (15)
$\langle^{2}d\rangle$	2.415	$\langle^{2}d\rangle$	2.418	$\langle^{3}d\rangle$	2.548
^{2}ECoN	3.000	^{2}ECoN	3.000	^{3}ECoN	3.075
Ag2—S7	2.4912 (18)	Ag3—S4	2.5241 (19)	Ag4/Cu4′—S5	2.4340 (19)
Ag2—S9/Se9′	2.507 (2)	Ag3—S9/Se9′	2.5856 (18)	Ag4/Cu4′—S9/Se9′	2.4472 (19)
Ag2—S8	2.6046 (18)	Ag3—S6	2.5982 (17)	Ag4/Cu4′—S4	2.485 (2)
Ag2—S2/Se2′	3.0425 (15)	Ag3—S2/Se2′	3.0414 (14)		
$\langle^{4}d\rangle$	2.551	$\langle^{4}d\rangle$	2.594	$\langle^{2}d\rangle$	2.457
^{4}ECoN	3.273	^{4}ECoN	3.372	^{2}ECoN	3.008
Ag5/Cu5′—S8	2.4366 (18)	Ag6—S3	2.534 (2)		
Ag5/Cu5′—S3	2.481 (2)	Ag6—S7	2.5700 (17)		
Ag5/Cu5′—S9/Se9′	2.4945 (19)	Ag6—S9/Se9′	2.5917 (18)		
Ag5/Cu5′—S1/Se1′	2.9319 (16)	Ag6—S1/Se1′	3.0095 (14)		
$\langle^{4}d\rangle$	2.494	$\langle^{4}d\rangle$	2.593		
^{4}ECoN	3.368	^{4}ECoN	3.431		
$[Ag_9Cu(S,Se)_2Se_2]^{2+}$ *B* layer (in increasing ^{n}ECoN for Ag):					
Ag15—S2/Se2′	2.5360 (15)	Ag13—S1/Se1′	2.5702 (15)	Ag12—S4	2.524 (2)
Ag15—Se1	2.5461 (9)	Ag13—Se1	2.6216 (9)	Ag12—Se1	2.8454 (9)
Ag15—S5	2.8539 (18)	Ag13—S6	2.7549 (18)	Ag12—Se2	2.6767 (9)
		Ag13—S5	3.4016 (19)	Ag12—S2/Se2′	3.0869 (14)
		Ag13—Se1	3.4055 (10)		
$\langle^{4}d\rangle$	2.595	$\langle^{4}d\rangle$	2.648	$\langle^{6}d\rangle$	2.675
^{4}ECoN	2.717	^{4}ECoN	3.062	^{6}ECoN	3.230
Ag7—S8	2.6414 (18)	Ag9—S1/Se1′	2.5641 (15)	Ag10—S3	2.635 (2)
Ag7—Se2	2.7299 (9)	Ag9—Se2	2.6184 (9)	Ag10—Se2	2.6971 (10)
Ag7—S2/Se2′	2.7516 (6)	Ag9—S8	2.9328 (18)	Ag10—S1/Se1′	2.7231 (15)
Ag7—Se2	3.2691 (9)	Ag9—S7	3.0201 (18)	Ag10—Se1	3.0704 (11)
$\langle^{4}d\rangle$	2.726	$\langle^{6}d\rangle$	2.686	$\langle^{4}d\rangle$	2.717
^{4}ECoN	3.260	^{6}ECoN	3.291	^{4}ECoN	3.555
Ag11—S1/Se1′	2.5617 (15)	Ag14—S2/Se2′	2.6463 (15)	Ag8—S7	2.6370 (18)
Ag11—Se1	2.6012 (9)	Ag14—S6	2.7125 (18)	Ag8—Se2	2.7157 (9)
Ag11—S5	2.8353 (19)	Ag14—Se1	2.7130 (9)	Ag8—S2/Se2′	2.7230 (15)
Ag11—S3	2.923 (2)	Ag14—Se1	2.9648 (9)	Ag8—Se2	2.8998 (10)
$\langle^{5}d\rangle$	2.674	$\langle^{3}d\rangle$	2.725	$\langle^{3}d\rangle$	2.723
^{5}ECoN	3.568	^{3}ECoN	3.750	^{3}ECoN	3.836
Cu1—S2/Se2′	2.1951 (14)				
Cu1—S1/Se1′	2.2024 (15)				
$\langle^{2}d\rangle$	2.199				
^{2}ECoN	2.000				

Shortest cation–cation distances: Ag—Cu: 2.7971 (9) Å, Ag—Ag: 2.8812 (10) Å.

symmetry). In the 221-polybasite there are two different arrangements around Cu atoms (highlighted by the thin connecting line in Fig. 4), whereas in Se-rich antimonpearceite there is only one pattern, thus causing symmetry and cell metric differences.

As is sometime the case when dealing with d^{10} cations, such as Ag^{+} or Cu^{+}, the structure description in terms of simple polyhedra is difficult, if even possible. Indeed, for such cations there is not a clear distinction between the bonding and non-bonding distances since the coordinating atoms are at distances which span a large interval, defining highly distorted polyhedra with preferentially low coordination d^{10} environments. Gaudin *et al.* (2001) pointed out by means of FLAPW band structure calculations that the factors influencing the low coordination are the metal *s*/*d* orbital mixing and the d^{10} element polarization. In the Se-rich antimonpearceite the situation is made even more complex with the presence of pure S or Se and mixed S/Se sites in the d^{10} cation coordination sphere. Since the coordination number cannot be straightforwardly given as an integer number, a solution consists of using the weighted mean distance, $\langle^{n}d(ij\Rightarrow r)\rangle$, hereafter referred to as ^{n}WMD, and the effective coordination number, ^{n}ECoN, as defined by Hoppe (1979) and Nespolo *et al.* (2001), obtained through the scaling of each bond distance to the shortest bond length of each polyhedron (instead of an empirical normalization parameter used in the classical bond valence analysis). These parameters have been calculated for each cation using the *Chardi-IT* program (Nespolo *et al.*, 2001) and are gathered in Table 4, along with the interatomic distances calculated using the *Jana2000* program. Note that the charge distribution could not be calculated since the Chardi–IT program cannot handle a large number of independent atoms in its present version. In the following sections, in the case of an M/M' partial substitution, a site will be referred to by its major component (that is M), except when the $M \Rightarrow M'$ substitution brings noticeable modifications upon the distances and/or the coordination with neighbouring atoms (it is then referred to as M/M' to highlight the role of the minor element in the substitution).

In the $[(Ag,Cu)_6(Sb,As)_2(S,Se)_7]^{2-}$ *A* (or *A*′) module layer, the arrangement is the same as in pearceite (Bindi *et al.*, 2006) and in the 222- and 221-polybasite (Evain *et al.*, 2006), as illustrated in Fig. 5. Each silver cation has a sulfur (or mixed S/Se) threefold coordination, although slightly out of the S3 triangle and establishing a very weak bond with an additional S atom of the *B* (or *B*′) module layer (as shown in Table 4 with ^{n}ECoN values greater than 3.0, but not shown in Fig. 5). Two Ag—S weighted mean distances are shorter (2.457 and 2.494 Å) than the other four Ag—S weighted mean distances (ranging from 2.548 to 2.594 Å), in agreement with the partial substitution of Ag by Cu in those two sites. Similarly, the calculated Ag—S weighted mean distances are slightly longer than those observed for the 222-polybasite (2.476 *versus* 2.416 Å for Ag/Cu and 2.572 *versus* 2.530 Å for pure Ag), in agreement with the partial substitution of S by Se

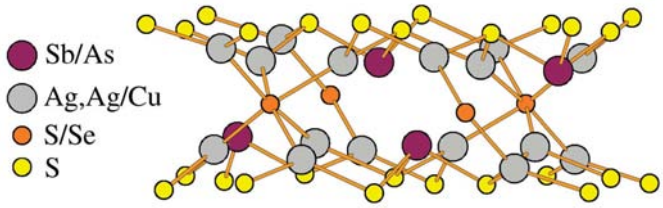

Figure 5
The connection between the $[AgS_3]^{5-}$ triangular units and the $[SbS_3]^{3-}$ pyramids in the $[(Ag,Cu)_6(Sb,As)_2(S,Se)_7]^{2-}$ *A* (*A*′) module layer of Se-rich antimonpearceite. The mixed S/Se site in the middle of the module layer is highlighted by a specific color.

in all Ag coordination spheres. Each $[AgS_3]^{5-}$ unit is linked either to five other $[AgS_3]^{5-}$ units by sharing a common sulfur apex or to a single $[AgS_3]^{5-}$ unit and a $[SbS_3]^{3-}$ pyramid (see Fig. 5). In the $[SbS_3]^{3-}$ pyramid, the mean ⟨Sb—S⟩ bond distance (2.417 Å) is equal to the average ^{n}WMD and is consistent with the value obtained by considering the ⟨Sb—S⟩ bonds of pyrargyrite, $Ag_3[SbS_3]$ (2.452 Å; Engel & Nowacki, 1966), given the partial substitution of Sb by As. One should note that the mixed S/Se site is the site, in the middle of the layer, connecting the $[AgS_3]^{5-}$ units and that none of the outer S atoms are partially substituted by selenium. Therefore, the Sb atoms are surrounded by pure S-atom sites.

In the $[Ag_9Cu(S,Se)_2Se_2]^{2+}$ *B* (or *B*′) module layer, the nine independent Ag atoms adopt various coordinations extending from quasi-linear to quasi-tetrahedral (see Fig. 1*b*). Whatever the coordination, each Ag atom includes one pure Se in its close environment. Contrary to what is observed for 222- or 221-polybasite, no Ag atom can be considered in a 'true' linear environment (with ^{n}ECoN value close to 2.0), the closest to linear coordination being Ag15 with an S—Ag—Se angle of ∼162° and a third atom entering the polyhedron at a longer distance (see Table 4). Then coordinations evolve from close to threefold coordination (Ag13, Ag12 and Ag7) to pure tetrahedral (Ag8). Finally, Cu1 shows a 'true' linear coordination with Cu—S distances [⟨Cu—S/Se⟩ = 2.20 Å] slightly longer than those observed in 222- and 221-polybasite (2.16 Å) because of the partial substitution of both coordinating S atoms by Se atoms.

5. Concluding remarks

The structure determination of both the higher- and lower-temperature forms of the Se-rich antimonpearceite has revealed similarities and differences with respect to the pearceite and 222- and 221-polybasite structures. In the higher-temperature ionic-conducting form, the structure resembles that of all compounds of the pearceite/polybasite group in their higher-temperature form (*i.e.* 111 pearceite-type structure). The real difference is the presence of a pure Se site and of partially substituted S/Se sites. In the lower-temperature form, the Se-rich antimonpearceite differs from the 222-polybasite phase by its cell, symmetry and arrangement within the *B* (*B*′) module layer. It is worth noting that those differences do not clearly appear in the diffraction pattern since it can be indexed with a 222 cell if one does not take into account the twinning. It is quite possible that some pearceite or polybasite compounds containing amounts of selenium in substitution might present a different structure, namely the 222- or 221-polybasite structure. Only a complete structure determination including the twinning can then lift the ambiguity.

The authors are grateful to Professor Paul G. Spry (Iowa State University, USA) for his help in electron microprobe analyses. This work was funded by CNR (Istituto di Geoscienze e Georisorse, sezione di Firenze) and by MIUR, PRIN 2005 project 'Complexity in Minerals: Modulation, Modularity, Structural Disorder'.

References

Becker, P. J. & Coppens, P. (1974). *Acta Cryst.* A**30**, 129–147.
Bindi, L., Evain, M. & Menchetti, S. (2006). *Acta Cryst.* B**62**, 212–219.
Boucher, F., Evain, M. & Brec, R. (1992). *J. Solid State Chem.* **100**, 341–355.
Boucher, F., Evain, M. & Brec, R. (1993). *J. Solid State Chem.* **107**, 332–346.
Brandenburg, K. (2001). *Diamond.* Version 3. Crystal Impact GbR, Bonn, Germany.
Edenharter, A., Koto, K. & Nowacki, W. (1971). *N. Jahr. Mineral. Monatsh.* pp. 337–341.
Engel, P. & Nowacki, W. (1966). *N. Jah. Miner. Monatsh.* pp. 181–195.
Evain, M., Bindi, L. & Menchetti, S. (2006). *Acta Cryst.* B**62**, 447–456.
Frondel, C. (1963). *Am. Miner.* **48**, 565–572.
Gaudin, E., Boucher, F. & Evain, M. (2001). *J. Solid State Chem.* **160**, 212–221.
Hall, H. T. (1967). *Am. Miner.* **52**, 1311–1321.
Harris, D. C., Nuffield, E. W. & Frohberg, M. H. (1965). *Can. Miner.* **8**, 172–184.
Herrendorf, W. (1993). PhD dissertation, University of Karlsruhe, Germany.
Hoppe, R. (1979). *Z. Kristallogr.* **150**, 23–52.
Johnson, C. K. & Levy, H. A. (1974). *International Tables for X-ray Crystallography*, edited by J. A. Ibers & W. C. Hamilton, Vol. IV, pp. 311–336. Birmingham: Kynoch Press.
Kuhs, W. F. & Heger, G. (1979). *Fast Ion Transport in Solids*, edited by P. Vashishta, J. N. Mundy & G. K. Shenoy, pp. 233–236. Amsterdam: Elsevier.
Minčeva-Stefanova, I. (1979). *Dokl. Bolgar. Akad. Nauk*, **32**, 501–504.
Nespolo, M. (2004). *Z. Kristallogr.* **219**, 57–71.
Nespolo, M., Ferrairs, G., Ivaldi, G. & Hoppe, R. (2001). *Acta Cryst.* B**57**, 652–664.
Petricek, V. & Dusek, M. (2000). *JANA2000, A Crystallographic Computing System.* Institute of Physics, Academy of Sciences of the Czech Republic, Prague, Czech Republic.
Spek, A. L. (1990). *PLATON, A Multipurpose Crystallographic Tool.* Ultrecht University, Ultrecht, The Netherlands.
Stoe & Cie (1996). *X-shape.* Version 1.02. Stoe and Cie, Darmstadt, Germany.